

UC Berkeley

UC Berkeley Previously Published Works

Title

Evidence for quantum spin liquid behaviour in single-layer 1T-TaSe₂ from scanning tunnelling microscopy

Permalink

<https://escholarship.org/uc/item/0571n4tq>

Journal

Nature Physics, 17(10)

ISSN

1745-2473

Authors

Ruan, Wei
Chen, Yi
Tang, Shujie
[et al.](#)

Publication Date

2021-10-01

DOI

10.1038/s41567-021-01321-0

Peer reviewed

1 **Evidence for quantum spin liquid behavior in single-layer 1T-TaSe₂**
2 **from scanning tunneling microscopy**

3
4 Wei Ruan^{1,2,†}, Yi Chen^{1,2,†}, Shujie Tang^{3,4,5,6,7}, Jinwoong Hwang^{5,8}, Hsin-Zon Tsai^{1,10}, Ryan L.
5 Lee¹, Meng Wu^{1,2}, Hyejin Ryu^{5,9}, Salman Kahn¹, Franklin Liou¹, Caihong Jia^{1,2,11}, Andrew
6 Aikawa¹, Choongyu Hwang⁸, Feng Wang^{1,2,12}, Yongseong Choi¹³, Steven G. Louie^{1,2}, Patrick
7 A. Lee¹⁴, Zhi-Xun Shen^{3,4}, Sung-Kwan Mo⁵, Michael F. Crommie^{1,2,12,*}

8
9 ¹*Department of Physics, University of California, Berkeley, California 94720, USA*

10 ²*Materials Sciences Division, Lawrence Berkeley National Laboratory, Berkeley, California*
11 *94720, USA*

12 ³*Stanford Institute for Materials and Energy Sciences, SLAC National Accelerator*
13 *Laboratory and Stanford University, Menlo Park, California 94025, USA*

14 ⁴*Geballe Laboratory for Advanced Materials, Departments of Physics and Applied Physics,*
15 *Stanford University, Stanford, California 94305, USA*

16 ⁵*Advanced Light Source, Lawrence Berkeley National Laboratory, Berkeley, California*
17 *94720, USA*

18 ⁶*CAS Center for Excellence in Superconducting Electronics, Shanghai Institute of*
19 *Microsystem and Information Technology, Chinese Academy of Sciences, Shanghai 200050,*
20 *China*

21 ⁷*School of Physical Science and Technology, Shanghai Tech University, Shanghai 200031,*
22 *China*

23 ⁸*Department of Physics, Pusan National University, Busan 46241, Korea*

24 ⁹*Center for Spintronics, Korea Institute of Science and Technology, Seoul 02792, Korea*

25 ¹⁰*International Collaborative Laboratory of 2D Materials for Optoelectronic Science &*
26 *Technology of Ministry of Education, Engineering Technology Research Center for 2D*
27 *Material Information Function Devices and Systems of Guangdong Province, Shenzhen*
28 *University, Shenzhen 518060, China*

29 ¹¹*Henan Key Laboratory of Photovoltaic Materials and Laboratory of Low-dimensional*
30 *Materials Science, School of Physics and Electronics, Henan University, Kaifeng 475004,*
31 *China*

32 ¹²*Kavli Energy Nano Sciences Institute at the University of California Berkeley and the*
33 *Lawrence Berkeley National Laboratory, Berkeley, California 94720, USA*

34 ¹³*Advanced Photon Source, Argonne National Laboratory, Argonne, Illinois 60439, USA*

35 ¹⁴*Department of Physics, Massachusetts Institute of Technology, Cambridge MA 02139, USA*

36 † *These authors contributed equally to this work.*

37 **e-mail: crommie@berkeley.edu*

38

39 **Abstract**

40 Two-dimensional triangular-lattice antiferromagnets are predicted under some
41 conditions to exhibit a quantum spin liquid ground state with no energy barrier to creating
42 emergent, fractionalized spinon excitations that carry spin but no charge. Materials that
43 realize this kind of spin liquid are expected to have low-energy behavior described by a
44 spinon Fermi surface. Directly imaging the resulting spinons, however, is difficult due to
45 their chargeless nature. Here we use scanning tunneling spectroscopy to image density waves
46 consistent with predictions of spinon density modulation arising from a spinon Fermi surface
47 instability in single-layer 1T-TaSe₂. We confirm the existence of a triangular lattice of
48 localized spins in this material by contacting it to a metallic 1H-TaSe₂ substrate and
49 measuring the Kondo effect. Spectroscopic imaging of isolated single-layer 1T-TaSe₂ reveals
50 long-wavelength super-modulations at Hubbard band energies, consistent with the predicted
51 behavior of itinerant spinons. These super-modulations allow direct experimental
52 measurement of the spinon Fermi wavevector, in good agreement with theoretical predictions
53 for a two-dimensional quantum spin liquid.

54

55 Since the first predictions by Anderson in 1973¹, quantum spin liquids (QSLs) have
56 been intensely investigated²⁻⁷ as candidates to host exotic quantum phenomena such as
57 fractionalized elementary excitations²⁻⁴, topological order^{4,5}, and unconventional
58 superconductivity^{6,7}. QSLs are a novel state of matter predicted to arise in quantum
59 antiferromagnets where geometric frustration and quantum fluctuations are strong enough to
60 prevent a magnetically ordered ground state²⁻⁴. A key to understanding the QSL state is its
61 low-energy physics, often dominated by emergent fractional fermions (termed spinons) that
62 carry spin-1/2 but no charge²⁻⁴. Many QSL models are based on two-dimensional (2D)
63 triangular-lattice Mott insulators²⁻⁴, and several material candidates incorporating coupled 2D
64 layers have been found to exhibit behavior consistent with spinon excitations⁸⁻¹⁰. It remains
65 debatable whether the spinons in such systems are gapped or not^{4,8-10}, but increasing
66 evidence¹⁰ suggests the existence of gapless spinons that exhibit a Fermi surface^{2-4,8-13}.

67 Imaging the itinerant spinons, however, is challenging due to their fractional and
68 chargeless nature. Some predictions suggest that the spinon Fermi surface should host
69 instabilities leading to spinon spatial patterns¹³ that can, in principle, be imaged by single-
70 particle scanned probes¹⁴. Bulk 1T-TaS₂ has been suggested as one such QSL candidate¹⁵⁻²¹.
71 This layered material is believed to exhibit a Mott insulator ground state that arises
72 cooperatively from a star-of-David charge density wave (CDW)²²⁻²⁴. Each star-of-David
73 cluster contributes one localized spin, thus forming a triangular spin lattice. Some evidence
74 for QSL behavior in bulk 1T-TaS₂ has been found, such as the absence of magnetic order
75 down to millikelvin temperature¹⁷⁻¹⁹ and a linear term in the thermal conductivity^{20,21}, but
76 QSL physics here is complicated by interlayer coupling. This is because interlayer coupling
77 can lead to spin delocalization and/or interlayer spin-singlet formation, which are detrimental
78 to forming a gapless QSL state^{15,19,25-27}.

79 Here we report experimental evidence supporting the existence of a QSL-based

80 spinon Fermi surface in single-layer (SL) 1T-TaSe₂ through the use of scanning tunneling
81 microscopy/spectroscopy (STM/STS). SL 1T-TaSe₂ is a newly discovered 2D Mott insulator
82 that exhibits a low-temperature star-of-David CDW phase similar to bulk 1T-TaS₂ (i.e., the
83 star-of-David cells are centered at Ta atoms - Supplementary Fig. 1), but which does not
84 suffer from the disadvantages of interlayer coupling between 1T layers^{28,29}. We report two
85 experimental findings that support the presence of a QSL in SL 1T-TaSe₂. First we
86 demonstrate the existence of localized spins on a triangular lattice in SL 1T-TaSe₂ through
87 the observation of a Kondo resonance at the Fermi level (E_F) when SL 1T-TaSe₂ is placed in
88 contact with metallic 1H-TaSe₂. Next we show evidence for a QSL-based spinon Fermi
89 surface subject to a Fermi surface instability in isolated SL 1T-TaSe₂ through the observation
90 of long-wavelength super-modulations in the electronic local density of states (LDOS) at the
91 Hubbard band energies. Such wave patterns are unexpected in an insulator but occur naturally
92 in the presence of a spinon Fermi surface. The ability to access fractional spinon behavior via
93 a single-particle probe (i.e., STM) arises from the decomposition of injected electrons into
94 spinons (chargeless spin-1/2 fractional particles) and chargons (spinless charged fractional
95 particles)^{14,30}. By imaging spinon-induced LDOS super-modulations we are able to directly
96 determine the spinon Fermi wavevector (k_F), in good agreement with theoretical
97 predictions^{15,16} for a 2D QSL.

98 **Kondo resonance in a 1T/1H TaSe₂ vertical heterostructure**

99 SL TaSe₂ films were grown on epitaxial bilayer graphene (BLG) terminated 6H-
100 SiC(0001) substrates and also on cleaved graphite surfaces via molecular beam epitaxy
101 (MBE)^{29,31}. A single layer of TaSe₂ contains one Ta atomic layer sandwiched between a pair
102 of Se atomic layers, with each Ta atom coordinated by six Se atoms (Fig. 1a). The Se cage
103 forms an octahedron in the metastable 1T-phase and a trigonal prism in the stable 1H-phase.
104 Coexisting 1T and 1H phases were grown via MBE in the SL limit under controlled growth

105 conditions, as shown by our STM images (Fig. 1b). Atomically-flat 1T and 1H SL islands can
106 easily be distinguished as seen by close-up images of both phases in the insets to Fig. 1b
107 which exhibit a triangular $\sqrt{13} \times \sqrt{13}$ star-of-David CDW pattern for the 1T-phase²⁹ and a 3
108 $\times 3$ CDW pattern for the 1H-phase³¹. Vertical heterostructures composed of a single 1T layer
109 on top of a single 1H layer (1T/1H) are observed to display the star-of-David CDW pattern in
110 the top layer and the 3×3 CDW in the bottom layer (Fig. 1b and Supplementary Fig. 2b).

111 We verified the electronic structure of the different TaSe₂ phases by measuring STM
112 differential conductance (dI/dV) (which reflects surface electronic LDOS) as a function of
113 sample bias voltage (V_b). dI/dV spectra acquired on metallic SL 1H-TaSe₂ islands show finite
114 LDOS at E_F accompanied by a slight suppression due to CDW formation (Fig. 2a green
115 curves), consistent with previous measurements³¹. dI/dV spectra acquired on insulating SL
116 1T-TaSe₂ islands on BLG/SiC, on the other hand, show a Mott gap (Fig. 2a red curves), also
117 consistent with previous measurements²⁹. Here the LDOS peak near $V_b = -0.3$ V is identified
118 as the lower Hubbard band (LHB) and the upper Hubbard band (UHB) corresponds to the
119 peaks near $V_b = 0.2$ V (UHB₁) and $V_b = 0.6$ V (UHB₂) (these are split due to reduced
120 screening in 2D²⁹). The electronic structure of both SL 1T and 1H phases was also identified
121 using angle-resolved photoemission spectroscopy (ARPES) (Supplementary Fig. 3b),
122 confirming the coexistence of both phases.

123 dI/dV spectra acquired on 1T/1H vertical heterostructures are very different from
124 either of the bare SL spectra at the Hubbard band energy scale. The heterostructure spectra
125 reveal a pronounced zero bias peak (ZBP) that is absent from single layers (Fig. 2a blue
126 curves) and which cannot be explained by doping³²⁻³⁵ or strain (Supplementary Note 2.1).
127 The ZBP was found to persist in every star-of-David cell (Supplementary Fig. 2). We identify
128 the ZBP as a Kondo resonance^{36,37}, which is expected to arise when a local spin (from the 1T
129 layer) couples to itinerant electrons in a metal (from the 1H layer)³⁸ (the absence of a Kondo

130 resonance for SL 1T-TaSe₂ on BLG is due to BLG's low carrier density and poor coupling to
 131 the 1T layer (Supplementary Note 2.2)). To test the Kondo hypothesis we examined the ZBP
 132 feature over the temperature range $5 \text{ K} \leq T \leq 70 \text{ K}$, as plotted in Fig. 2b. The ZBP gradually
 133 broadens with increased temperature by an amount that cannot be accounted for by pure
 134 thermal broadening, but is well-fit by a thermally-convolved Fano line shape (Supplementary
 135 Note 2.3 and Supplementary Fig. 2d, e) with an intrinsic temperature-dependent width $\Gamma(T)$.
 136 The intrinsic resonance width as a function of temperature (T) is observed to follow the well-
 137 known Kondo expression³⁷

$$138 \quad \Gamma(T) = \sqrt{(\pi k_B T)^2 + 2(k_B T_K)^2} \#(1)$$

139 where k_B is the Boltzmann constant, yielding an estimated Kondo temperature of $T_K = 57 \pm 3$
 140 K (Fig. 2c, red dashed line) and a resultant Kondo-coupling of $J_K \approx 0.2 \text{ eV}$ (Supplementary
 141 Note 2.4). The observation of the Kondo resonance peak in every star-of-David CDW cell
 142 suggests the existence of localized spins in isolated SL 1T-TaSe₂ that are arranged in a
 143 triangular lattice (Fig. 1c) (this behavior is consistent with the typical lateral extension of
 144 Kondo peaks (which is on the order of 1 nm^{39}), as well as with the coherence temperature of
 145 the 1T/1H Kondo lattice being lower than the STM base temperature of 5 K (Supplementary
 146 Note 2.4)). Measuring magnetism in single-layer materials via more direct methods is
 147 challenging. For example, we attempted to probe magnetism in SL 1T-TaSe₂ using X-ray
 148 magnetic circular dichroism but this yielded no observable magnetization beyond the noise
 149 level (Supplementary Fig. 4).

150 **Super-modulations in single-layer 1T-TaSe₂**

151 We explored possible QSL behavior in isolated single layers of 1T-TaSe₂ (i.e., that
 152 are supported by BLG/SiC rather than the metallic 1H-TaSe₂ phase) by characterizing long-
 153 wavelength super-modulations in the real-space electronic structure of this triangular spin
 154 lattice (the Kondo effect plays no significant role for this material combination

155 (Supplementary Note 2.2)). Measurements were performed on SL 1T-TaSe₂ islands like the
 156 one shown in Fig. 3a which exhibit dI/dV spectra characteristic of a Mott insulator (Fig. 3b).
 157 Fig. 3c-g shows constant-height dI/dV maps acquired at different energies in the area outlined
 158 by a yellow dashed square in Fig. 3a, while Fig. 3h-l reveals the corresponding Fourier
 159 transform (FT) of each dI/dV map (see Supplementary Fig. 5 for FT images without labels).
 160 The star-of-David CDW pattern dominates the empty-state LDOS for energies above the
 161 UHB²⁹ as seen by the dI/dV map at $V_b = 1.0$ V in Fig. 3c and its FT in Fig. 3h. Here the CDW
 162 triangular lattice yields 6-fold symmetric FT peaks marked by red circles and labeled as the
 163 primary reciprocal lattice vectors \mathbf{b}_i ($1 \leq i \leq 6$). These define the first Brillouin zone of the
 164 star-of-David CDW (red hexagon). No other periodicities are seen at this energy.

165 New longer-wavelength super-modulations emerge at lower energies closer to the
 166 Hubbard band energies (i.e., UHB₂, UHB₁, and LHB). At energies near UHB₂ ($V_b = 0.62$ V),
 167 for example, a new super-modulation is clearly seen in the real-space image of Fig. 3d as
 168 bright patches of enhanced LDOS (see also Supplementary Fig. 6d). This structure
 169 corresponds to a triangular grid rotated by 30° from the CDW lattice with an incommensurate
 170 lattice constant slightly larger than $\sqrt{3}a$ (Supplementary Fig. 6) where a is the CDW lattice
 171 constant. This incommensurate super-modulation (ICS) is best seen in Fig. 3i (the FT of Fig.
 172 3d) which shows new peaks marked by blue circles along the Γ -K directions inside the CDW
 173 Brillouin zone. The ICS wavevector, \mathbf{q}_{ICS} , can be written in terms of the CDW reciprocal
 174 lattice vectors as $\mathbf{q}_{\text{ICS}} = q_{\text{ICS}}(\mathbf{b}_1 + \mathbf{b}_2)$ where $q_{\text{ICS}} = 0.241 \pm 0.009$ (q_{ICS} is obtained from
 175 Gaussian fits of FTs acquired on 10 different islands with 5 different tips - Supplementary
 176 Fig. 7).

177 The ICS pattern is also observed when energy is lowered further to UHB₁, as seen by
 178 the dI/dV map at $V_b = 0.2$ V (Fig. 3e) and corresponding FT (Fig. 3j). The ICS is often

179 obscured in real space images due to mixing with the CDW pattern (Supplementary Note 1),
 180 but its FT peaks are easily resolved from the CDW wavevectors (Fig. 3j). The ICS persists as
 181 energy is lowered to the LHB as seen in the dI/dV map at $V_b = -0.18$ V (Fig. 3f) which yields
 182 FT peaks at \mathbf{q}_{ICS} (Fig. 3k). The filled-state LHB measurement, however, differs from the
 183 empty-state UHB measurements in that it also exhibits a short-range commensurate super-
 184 modulation (CS) of wavelength $\sqrt{3}a$ that yields broad FT peaks at the K-points of the CDW
 185 Brillouin zone (green circles in Fig. 3k - see also Supplementary Fig. 8). Both the ICS and CS
 186 disappear at energies below the LHB where only the star-of-David CDW remains as shown
 187 by the dI/dV map at $V_b = -0.8$ V (Fig. 3g) and its corresponding FT (Fig. 3l).

188 The complete energy dependence of the super-modulations over the energy range -1V
 189 $< V_b < 1.5$ V is shown in Fig. 4a and b (Supplementary Figs. 9 and 10 show additional data at
 190 selected energies). Here the energy-dependent FT amplitude along the Γ -K direction (black
 191 dashed line in the inset to Fig. 4a) as a function of wavevector $\mathbf{q} = q(\mathbf{b}_1 + \mathbf{b}_2)$ shows three
 192 main features: (i) the CDW reciprocal lattice vector $\mathbf{b}_1 + \mathbf{b}_2$ ($q = 1$) over a wide energy range
 193 (black dashed ovals), (ii) the CS ($q = 1/3$) in the filled-state LHB (green dashed oval), and (iii)
 194 the ICS ($q = q_{\text{ICS}} \approx 1/4$) in both the LHB and UHB regimes (blue dashed ovals). We observe
 195 that the ICS wavevector is independent of energy, but its *amplitude* is not. To better visualize
 196 the energy dependence of the ICS amplitude, its strength is defined as the ICS FT peak
 197 amplitude $\rho(E, \mathbf{q}_{\text{ICS}})$ normalized by the FT peak amplitude $\rho(E, \mathbf{q} = \mathbf{0})$ (equivalent to the
 198 spatially averaged surface LDOS). Fig. 4b shows that this ratio, $|\rho(E, \mathbf{q}_{\text{ICS}})/\rho(E, \mathbf{q} = \mathbf{0})|$ (blue
 199 dots), is small at all energies except for the LHB and UHB regimes (a SL 1T-TaSe₂ dI/dV
 200 spectrum is plotted for reference (black line)). The temperature dependence of the ICS
 201 amplitude (Supplementary Fig. 11) shows that it decreases as temperature is raised and
 202 completely vanishes by $T = 77$ K, whereas the star-of-David CDW remains even up to room

203 temperature.

204 In order to investigate possible substrate effects on the behavior of the observed
205 super-modulation, SL 1T-TaSe₂ was also grown on cleaved graphite (HOPG) via MBE and
206 characterized by STM/STS. These samples also exhibit star-of-David CDW order and Mott
207 insulating behavior similar to films grown on BLG/SiC as shown by the STM images and
208 dI/dV spectra of Supplementary Fig. 12. STM images acquired in the LHB of SL 1T-
209 TaSe₂/HOPG and their FTs show the same ICS pattern as seen for SL 1T-TaSe₂/BLG/SiC
210 (Supplementary Fig. 12d and e). However, an additional 2×2 super-modulation (with
211 respect to the CDW lattice) is sometimes seen for SL 1T-TaSe₂/HOPG in the LHB that has
212 FT peaks near the M points (Fig. 5d and Supplementary Fig. 12f-k) (this was seen for 2 out of
213 11 islands). We refer to this new super-modulation wavevector as \mathbf{q}_M . \mathbf{q}_{ICS} and \mathbf{q}_M were never
214 simultaneously observed on the same SL 1T-TaSe₂/HOPG island.

215 **Relationship between super-modulations and QSL behavior**

216 Our experimental results support the hypothesis that SL 1T-TaSe₂ is a 2D QSL. The
217 first piece of evidence is that SL 1T-TaSe₂ contains a triangular lattice of localized spins, an
218 essential ingredient for a QSL. This evidence is provided by our observation of the Kondo
219 effect in 1T-layers supported by a 1H-layer, which implies that each star-of-David in isolated
220 SL 1T-TaSe₂ contains a single quantum spin (such Kondo screening does not occur when 1T-
221 layers are supported by graphene (Supplementary Note 2.2)). The second piece of evidence is
222 the long-wavelength super-modulations that we observe in SL 1T-TaSe₂ (when it is supported
223 by graphene) via STS imaging. These periodicities lie at the precise energies and wavevectors
224 expected for a QSL, as discussed below.

225 Before describing how these super-modulations are explained by QSL considerations,
226 however, we first rule out possible alternative explanations. The first alternative possibility is
227 electronic quasiparticle interference (QPI). Our observed ICS pattern is inconsistent with QPI

228 because its wavelength is energy independent over the Hubbard bandwidths. There are also
229 no significant electronic structure features at the Hubbard band edges that might induce a QPI
230 signal at \mathbf{q}_{ICS} (Supplementary Fig. 13). The second alternative possibility is a structural
231 distortion such as a moiré pattern and/or a surface reconstruction. This explanation is unlikely
232 because the observed super-modulations exist only over very specific energy ranges
233 involving the Hubbard bands, suggesting that they are electronic and/or spin-based
234 phenomena. To further exclude moiré patterns involving complex BLG/SiC reconstructions
235 we point to the fact that SL 1T-TaSe₂/HOPG exhibits the same ICS modulation as SL 1T-
236 TaSe₂/BLG/SiC (Supplementary Fig. 12). This is significant because HOPG has no
237 reconstruction and cannot combine with 1T-TaSe₂ to yield an ICS moiré pattern. We
238 additionally see no evidence of the super-modulation in low-energy electron diffraction
239 (LEED) patterns²⁹, and no evidence that it is a strain effect (Supplementary Note 3.1).
240 Reconstruction of the star-of-David CDW (i.e., subharmonic phonon softening) is also
241 unlikely since the star-of-David CDW is accounted for by *ab initio* calculations that show no
242 ICS distortion⁴⁰, and the temperature dependences of the ICS and the CDW are very different
243 (Supplementary Fig. 11). The last alternative possibility we will mention is Peierls-type or
244 correlation-driven charge order. The former typically requires an electron Fermi surface
245 while the latter usually appears at much lower energy scales than the Hubbard bands³². Such
246 behavior is inconsistent with the ICS observed in our system and has no reasonable
247 connection to the new periodicities seen here (i.e., \mathbf{q}_{ICS} and \mathbf{q}_{M}).

248 The presence of a QSL-based spinon Fermi surface, on the other hand, very naturally
249 explains both the energy-dependence and wavevectors of the \mathbf{q}_{ICS} and \mathbf{q}_{M} super-modulations
250 that we observe in SL 1T-TaSe₂. The starting point here is that our system hosts a QSL state
251 with a half-filled spinon band. This idea is supported by density matrix renormalization group

252 (DMRG) calculations based on the triangular-lattice t - J model with a ring exchange term that
 253 simulates the Hubbard model near a Mott transition¹⁶. In these calculations the spin-
 254 correlation peaks in the Γ -M directions are missing¹⁶ which suggests that a partial gap opens
 255 at the spinon Fermi wavevector k_F along the Γ -M directions due to a Fermi surface instability
 256 (the calculations, however, don't reveal the precise source of the instability - Fig. 5a). The
 257 value of the predicted spinon k_F comes from the spinon band structure which is modeled
 258 using a zero-flux mean-field tight-binding Hamiltonian¹⁰ with nearest-neighbor spinon
 259 hopping. This yields a value of the spinon Fermi wavevector in the Γ -M direction of $k_F \approx$
 260 0.375 reciprocal lattice units (r.l.u.) (inclusion of next-nearest-neighbor hopping does not
 261 significantly alter k_F – see Supplementary Note 3.2 and Supplementary Fig. 14).

262 The predicted instability of the spinon Fermi surface implies the existence of primary
 263 order wavevectors $\mathbf{P}_i = (1 - 2k_F)\mathbf{b}_i \approx 0.249\mathbf{b}_i$ that couple the gapped spinon Fermi surface
 264 regions in an extended zone scheme as shown in Fig. 5 (see red arrows in Fig. 5a and red dots
 265 in Fig. 5b). The absence of experimental LDOS super-modulations at these predicted
 266 wavevectors (Fig. 5c, d), however, suggests that the spinon Fermi surface instability is not a
 267 spinon density wave. Other candidates for the spinon Fermi surface instability, such as a
 268 spinon pair density wave^{13,41-43} or a spinon spin density wave, are more consistent with our
 269 experiment since they cannot be imaged directly by conventional STM because they reflect
 270 spatial modulations in either the spinon pair channel (in the case of spinon pair density wave)
 271 or the pure spin channel (in the case of spinon spin density wave). However, a *composite*
 272 spinon density wave that is observable by conventional STM can be induced at higher
 273 harmonics of the primary \mathbf{P}_i 's. This can be rationalized in a straightforward manner from
 274 either a scattering picture or a Landau formulation^{44,45} (Supplementary Notes 3.3, 3.4, and
 275 Supplementary Fig. 15).

276 We find that although the primary \mathbf{P}_i 's do not coincide with our observed super-
 277 modulation wavevectors, their higher harmonics (labeled \mathbf{Q}_i and \mathbf{Q}'_i in Fig. 5b) match our
 278 experimental super-modulations quite well. For example, the theoretical harmonics $\mathbf{Q}_i =$
 279 $\mathbf{P}_i + \mathbf{P}_{i+1} \approx 0.249(\mathbf{b}_i + \mathbf{b}_{i+1})$ match our experimentally measured super-modulations at
 280 $\mathbf{q}_{\text{ICS}} = (0.241 \pm 0.009)(\mathbf{b}_i + \mathbf{b}_{i+1})$ (Fig. 5c), while the theoretical harmonics $\mathbf{Q}'_i = 2\mathbf{P}_i$
 281 match our experimentally measured super-modulations at \mathbf{q}_M (Fig. 5d). Our experimental
 282 observation of the predicted harmonics at both \mathbf{Q}_i and \mathbf{Q}'_i strongly suggests the existence of a
 283 hidden primary wavevector \mathbf{P}_i and points to a spinon Fermi surface subject to instability at \mathbf{P}_i
 284 in SL 1T-TaSe₂.

285 If we work backwards and compare our measured value of $\mathbf{q}_{\text{ICS}} = q_{\text{ICS}}(\mathbf{b}_1 + \mathbf{b}_2)$ to
 286 the theoretically predicted composite spinon density wave vectors $\mathbf{Q}_i = \mathbf{P}_i + \mathbf{P}_{i+1}$ using
 287 $\mathbf{P}_i = (1 - 2k_F)\mathbf{b}_i$ then we find that the spinon Fermi wavevector can be written as $k_F =$
 288 $(1 - q_{\text{ICS}})/2$. This leads to an experimental value of $k_F = (0.380 \pm 0.005)$ r.l.u., in good
 289 agreement with the theoretically predicted value of $k_F = 0.375$ r.l.u. This value of k_F is also
 290 consistent with our ARPES data which shows enhanced intensity centered at Γ that greatly
 291 weakens for in-plane momenta beyond k_F (Supplementary Fig. 3). Our observed temperature
 292 dependence of the ICS feature is also consistent with this physical picture since it suggests a
 293 spinon Fermi surface instability transition at a temperature of $T \sim 60$ K (Supplementary Fig.
 294 11).

295 While the periodicities of our experimental super-modulations are well-explained by
 296 the QSL-based spinon scenario described above, a remaining question is how an STM that
 297 works by injecting charged particles (i.e., electrons) into a material can observe particles that
 298 have no charge (i.e., spinons). The answer lies in the process of fractionalization, whereby
 299 strongly correlated electrons in a QSL are predicted to separate into spinons (which have spin

300 and no charge) and chargons (which have charge and no spin). Due to constraints in the total
301 occupation of spinons and chargons, modulation of the spinon density can induce a small
302 density modulation of physical charge¹⁴. However, an even stronger effect occurs in the
303 tunneling process since an electron injected into the QSL UHB (or removed from the LHB)
304 will fractionalize into (or recombine from) a spinon and a chargon (see sketch in Fig. 4c and
305 d). The tunneling probability thus depends on both the spinon wavefunction and the chargon
306 wavefunction, and so the tunneling rate of an electron at a particular energy can be expressed
307 as a convolution of spinons and chargons that sum to the right energy, as done previously to
308 interpret ARPES data^{30,46} (Supplementary Note 3.5). Spatially periodic spinon density due to
309 modulations from a spinon Fermi surface instability should thus modulate quasiparticle
310 tunnel rates at the Hubbard band energies^{11-13,16} (Supplementary Note 3.5 and Supplementary
311 Fig. 16). Our experimental observation of long-wavelength super-modulations confined to
312 Hubbard band energies (Fig. 4a and b) supports this proposed mechanism whether the super-
313 modulations are thought to arise from a composite order picture or from scattering of spinons
314 (both of which are essentially equivalent as described in Supplementary Note 3.3 and 3.4).

315 Despite the agreement of our experimental results with the existence of a QSL spinon
316 Fermi surface, some mysteries remain. For instance, the \mathbf{P}_i vectors are also second harmonic
317 wavevectors of themselves (Supplementary Fig. 15b), and so their absence in our experiment
318 must be explained. One possible explanation is that this is a consequence of small structure
319 factors at \mathbf{P}_i (Supplementary Note 3.3). We note that the selective visibility of composite
320 density waves at higher harmonics has also been observed in other materials⁴⁷ and might be
321 affected by detailed defect and domain structure (Supplementary Fig. 12). Another open
322 question is the origin of the experimental CS pattern at the K-point wavevectors. The CS
323 pattern cannot be explained as a consequence of a spinon Fermi surface since K is not a
324 harmonic of the \mathbf{P}_i wavevectors. One possible explanation of the short-range CS is that our

325 QSL phase is close to an antiferromagnetic ordered phase in the phase diagram, thus causing
326 the CS to arise from short-range antiferromagnetic⁴⁸ fluctuations that are expected to be
327 commensurate with the K-points (Supplementary Note 4).

328 In conclusion, our STM measurements provide evidence that single-layer 1T-TaSe₂ is
329 a QSL with a spinon Fermi surface. Our observation of the Kondo effect in 1T-TaSe₂/1H-
330 TaSe₂ heterostructures implies that SL 1T-TaSe₂ exhibits a triangular spin lattice, and our
331 STS maps of 1T-TaSe₂ super-modulations directly reveal the effects of a spinon Fermi
332 surface instability in this material. Our experimentally determined value of the spinon Fermi
333 wavevector, $k_F = 0.380 \pm 0.005$ r.l.u., closely matches the theoretically predicted value of $k_F =$
334 0.375 r.l.u and supports the existence of a gapless QSL ground state. SL 1T-TaSe₂ thus
335 provides a new platform to further investigate QSL phenomena such as the response of 2D
336 QSLs to magnetic scatterers^{14,49,50} and electrostatic doping^{6,7,43}.

337 **Acknowledgments**

338 We thank Dung-Hai Lee, Joel E. Moore, and Michael Zaletel for helpful discussions.

339 **Funding:**

340 This research was supported by the VdW Heterostructure program (KCWF16)
341 (STM/STS measurements) and the Advanced Light Source (sample growth and ARPES)
342 funded by the Director, Office of Science, Office of Basic Energy Sciences, Materials
343 Sciences and Engineering Division, of the US Department of Energy under Contract No. DE-
344 AC02-05CH11231. Support was also provided by National Science Foundation award DMR-
345 1807233 (surface treatment and topographic characterization) and DMR-1926004 (theoretical
346 QPI analysis). The work at the Stanford Institute for Materials and Energy Sciences and
347 Stanford University (ARPES measurements) was supported by the DOE Office of Basic
348 Energy Sciences, Division of Material Science. The work at beamline 4-ID-D of the
349 Advanced Photon Source, Argonne National Laboratory (X-ray absorption measurements)

350 was supported by the DOE, Office of Science, Office of Basic Energy Sciences, under
351 Contract No. DEAC02-06CH11357. P.A.L. acknowledges support by DOE Basic Energy
352 Science award number DE-FG02-03ER46076 (theoretical QSL analysis). S. T. acknowledges
353 the support by CPSF-CAS Joint Foundation for Excellent Postdoctoral Fellows. J.H. and C.H.
354 acknowledge fellowship support from the NRF grant funded by the Korea government (MSIT)
355 (No. 2021R1A2C1004266). H.-Z.T. acknowledges fellowship support from the Shenzhen
356 Peacock Plan (Grant No. 827-000113, KQJSCX20170727100802505,
357 KQTD2016053112042971).

358 **Author Contributions:**

359 W.R., Y.C., P.A.L., and M.F.C. initiated and conceived this project. W.R., Y.C., R.L.,
360 H.-Z.T., S.K., F.L., C.J., and A.A. carried out STM/STS measurements under the supervision
361 of M.F.C. W.R., Y.C., F.W., P.A.L., and M.F.C. contributed to microscopy data analysis.
362 S.T., J. H., and H.R. performed sample growth and ARPES measurements/analysis under the
363 supervision of C.H., Z.-X.S., and S.-K.M. W.R., Y.C., R.L., and S.K. performed XMCD
364 measurements with support from Y Choi. M.W. performed DFT+U calculations under the
365 supervision of S.G.L. P.A.L. provided theoretical support. W.R., Y.C., and M.F.C. wrote the
366 manuscript with the help from all authors. All authors contributed to the scientific discussion.

367 **Competing interests:**

368 The authors declare no competing interests.

369

370 **Methods**

371 **Sample growth and ARPES measurements**

372 Both sample growth and ARPES measurements were performed at the HERS
373 endstation of Beamline 10.0.1, Advanced Light Source, Lawrence Berkeley National

374 Laboratory. Single-layer TaSe₂ films were grown on both BLG/6H-SiC(001) and HOPG
375 substrates in an ultrahigh-vacuum (UHV) MBE chamber under similar growth conditions as
376 described elsewhere²⁹. The substrate temperature was set at 660 °C, much higher than that for
377 the growth of pure 1H-TaSe₂, to allow a simultaneous growth of single-layer 1T-TaSe₂ and
378 single-layer 1H-TaSe₂, as well as vertical heterostructures composed of a 1T layer on top of a
379 1H layer. After growth, the samples were transferred in-situ into the analysis chamber with a
380 base pressure 3×10^{-11} Torr for ARPES measurements at 12 K. The photon energy was set at
381 50 eV with energy and angular resolution of 12 meV and 0.1°, respectively. The samples
382 were then capped by Se capping layers with ~10 nm thickness for protection during transport
383 through air to the UHV STM chamber.

384 **STM/STS measurements**

385 STM and STS measurements were performed in a low-temperature ultrahigh-vacuum
386 STM system (CreaTec) at $T = 5$ K (unless specified otherwise). Prior to measurements, the
387 samples were annealed in UHV at ~200 °C for 3 hours to remove the Se capping layers and
388 then immediately transferred in-situ into the STM stage sitting at $T = 5$ K. Electrochemically
389 etched tungsten tips were calibrated on a Au(111) surface before measurements. dI/dV
390 spectra were collected using standard lock-in techniques ($f = 401$ Hz). dI/dV mapping was
391 performed in constant-height mode (i.e., with the feedback loop open).

392 **XMCD measurements**

393 XMCD measurements were performed at beamline 4-ID-D, Advanced Photon Source,
394 Argonne National Laboratory. Hard X-ray was used to probe Ta L₂ and L₃ edges at grazing
395 incident angles to optimize the signal from single-layer 1T-TaSe₂ relative to background
396 noise from the substrate. Absorption spectra were collected in fluorescence yield mode. SL
397 1T-TaSe₂/BLG samples were capped with Se layers during transport to the XMCD
398 measurement chambers. The samples were mounted with the sample plane in the vertical

399 direction. The X-ray beam size was adjusted to be 0.1 mm along the horizontal direction and
400 0.3 mm along the vertical direction.

401 **Data availability:**

402 The data presented in Figs. 1-5 are available with the paper. All other data that
403 support the findings of this study are available from the corresponding authors upon
404 reasonable request.

405 **Code availability:**

406 The codes used in this study are available from the corresponding author upon
407 reasonable request.

408

409 **References**

- 410 1 Anderson, P. W. Resonating valence bonds: a new kind of insulator? *Mat. Res. Bull.* **8**,
411 153-160 (1973).
- 412 2 Lee, P. A. An End to the Drought of Quantum Spin Liquids. *Science* **321**, 1306-1307
413 (2008).
- 414 3 Balents, L. Spin liquids in frustrated magnets. *Nature* **464**, 199-208 (2010).
- 415 4 Zhou, Y., Kanoda, K. & Ng, T.-K. Quantum spin liquid states. *Rev. Mod. Phys.* **89**,
416 025003 (2017).
- 417 5 Wen, X.-G. Quantum orders and symmetric spin liquids. *Phys. Rev. B* **65**, 165113
418 (2002).
- 419 6 Anderson, P. W. The Resonating Valence Bond State in La_2CuO_4 and
420 Superconductivity. *Science* **235**, 1196-1198 (1987).
- 421 7 Lee, P. A. From high temperature superconductivity to quantum spin liquid: progress
422 in strong correlation physics. *Rep. Prog. Phys.* **71**, 012501 (2008).
- 423 8 Shimizu, Y., Miyagawa, K., Kanoda, K., Maesato, M. & Saito, G. Spin liquid state in
424 an organic Mott insulator with a triangular lattice. *Phys. Rev. Lett.* **91**, 107001 (2003).
- 425 9 Yamashita, M. *et al.* Highly Mobile Gapless Excitations in a Two-Dimensional
426 Candidate Quantum Spin Liquid. *Science* **328**, 1246-1248 (2010).
- 427 10 Shen, Y. *et al.* Evidence for a spinon Fermi surface in a triangular-lattice quantum-
428 spin-liquid candidate. *Nature* **540**, 559-562 (2016).
- 429 11 Motrunich, O. I. Variational study of triangular lattice spin-1/2 model with ring
430 exchanges and spin liquid state in $\kappa\text{-(ET)}_2\text{Cu}_2(\text{CN})_3$. *Phys. Rev. B* **72**, 045105 (2005).
- 431 12 Lee, S. S. & Lee, P. A. U(1) gauge theory of the Hubbard model: spin liquid states
432 and possible application to $\kappa\text{-(BEDT-TTF)}_2\text{Cu}_2(\text{CN})_3$. *Phys. Rev. Lett.* **95**, 036403
433 (2005).
- 434 13 Lee, S. S., Lee, P. A. & Senthil, T. Amperean pairing instability in the U(1) spin
435 liquid state with fermi surface and application to $\kappa\text{-(BEDT-TTF)}_2\text{Cu}_2(\text{CN})_3$. *Phys.*
436 *Rev. Lett.* **98**, 067006 (2007).

- 437 14 Mross, D. F. & Senthil, T. Charge Friedel oscillations in a Mott insulator. *Phys. Rev. B* **84**, 041102(R) (2011).
- 438
- 439 15 Law, K. T. & Lee, P. A. 1T-TaS₂ as a quantum spin liquid. *Proc. Natl. Acad. Sci. U. S. A.* **114**, 6996-7000 (2017).
- 440
- 441 16 He, W. Y., Xu, X. Y., Chen, G., Law, K. T. & Lee, P. A. Spinon Fermi Surface in a Cluster Mott Insulator Model on a Triangular Lattice and Possible Application to 1T-TaS₂. *Phys. Rev. Lett.* **121**, 046401 (2018).
- 442
- 443
- 444 17 Klanjšek, M. *et al.* A high-temperature quantum spin liquid with polaron spins. *Nature Phys.* **13**, 1130-1134 (2017).
- 445
- 446 18 Kratochvilova, M. *et al.* The low-temperature highly correlated quantum phase in the charge-density-wave 1T-TaS₂ compound. *npj Quantum Materials* **2**, 42 (2017).
- 447
- 448 19 Ribak, A. *et al.* Gapless excitations in the ground state of 1T-TaS₂. *Phys. Rev. B* **96**, 195131 (2017).
- 449
- 450 20 Yu, Y. J. *et al.* Heat transport study of the spin liquid candidate 1T-TaS₂. *Phys. Rev. B* **96**, 081111(R) (2017).
- 451
- 452 21 Murayama, H. *et al.* Effect of quenched disorder on the quantum spin liquid state of the triangular-lattice antiferromagnet 1T-TaS₂. *Phys. Rev. Research* **2**, 013099 (2020).
- 453
- 454 22 Wilson, J. A., Di Salvo, F. J. & Mahajan, S. Charge-density waves and superlattices in the metallic layered transition metal dichalcogenides. *Adv. Phys.* **24**, 117-201 (1975).
- 455
- 456
- 457 23 Fazekas, P. & Tosatti, E. Electrical, structural and magnetic properties of pure and doped 1T-TaS₂. *Philos. Mag.* **39**, 229-244 (1979).
- 458
- 459 24 Qiao, S. *et al.* Mottness Collapse in 1T-TaS_{2-x}Se_x Transition-Metal Dichalcogenide: An Interplay between Localized and Itinerant Orbitals. *Phys. Rev. X* **7**, 041054 (2017).
- 460
- 461 25 Ritschel, T. *et al.* Orbital textures and charge density waves in transition metal dichalcogenides. *Nature Phys.* **11**, 328-331 (2015).
- 462
- 463 26 Ma, L. *et al.* A metallic mosaic phase and the origin of Mott-insulating state in 1T-TaS₂. *Nat. Commun.* **7**, 10956 (2016).
- 464
- 465 27 Cho, D. *et al.* Nanoscale manipulation of the Mott insulating state coupled to charge order in 1T-TaS₂. *Nat. Commun.* **7**, 10453 (2016).
- 466
- 467 28 Nakata, Y. *et al.* Selective Fabrication of Mott-Insulating and Metallic Monolayer TaSe₂. *ACS Appl. Nano Mater.* **1**, 1456-1460 (2018).
- 468
- 469 29 Chen, Y. *et al.* Strong correlations and orbital texture in single-layer 1T-TaSe₂. *Nature Phys.* **16**, 218-224 (2020).
- 470
- 471 30 Kim, B. J. *et al.* Distinct spinon and holon dispersions in photoemission spectral functions from one-dimensional SrCuO₂. *Nature Phys.* **2**, 397-401 (2006).
- 472
- 473 31 Ryu, H. *et al.* Persistent Charge-Density-Wave Order in Single-Layer TaSe₂. *Nano Lett.* **18**, 689-694 (2018).
- 474
- 475 32 Cai, P. *et al.* Visualizing the evolution from the Mott insulator to a charge-ordered insulator in lightly doped cuprates. *Nature Phys.* **12**, 1047-1051 (2016).
- 476
- 477 33 Ruan, W. *et al.* Relationship between the parent charge transfer gap and maximum transition temperature in cuprates. *Science Bulletin* **61**, 1826-1832 (2016).
- 478
- 479 34 Battisti, I. *et al.* Universality of pseudogap and emergent order in lightly doped Mott insulators. *Nature Phys.* **13**, 21-25 (2017).
- 480
- 481 35 Ruan, W. *et al.* Visualization of the periodic modulation of Cooper pairing in a cuprate superconductor. *Nature Phys.* **14**, 1178-1182 (2018).
- 482
- 483 36 Hewson, A. C. *The Kondo Problem to Heavy Fermions*. (The Press Syndicate of the University of Cambridge, 1993).
- 484
- 485 37 Nagaoka, K., Jamneala, T., Grobis, M. & Crommie, M. F. Temperature dependence

486 of a single Kondo impurity. *Phys. Rev. Lett.* **88**, 077205 (2002).
 487 38 Helmes, R. W., Costi, T. A. & Rosch, A. Kondo proximity effect: how does a metal
 488 penetrate into a Mott insulator? *Phys. Rev. Lett.* **101**, 066802 (2008).
 489 39 Madhavan, V. V., Chen, W., Jamneala, T., Crommie, M. F. & Wingreen, N. S.
 490 Tunneling into a Single Magnetic Atom: Spectroscopic Evidence of the Kondo
 491 Resonance. *Science* **280**, 567-569 (1998).
 492 40 Ge, Y. & Liu, A. Y. First-principles investigation of the charge-density-wave
 493 instability in 1T-TaSe₂. *Phys. Rev. B* **82**, 155133 (2010).
 494 41 Galitski, V. & Kim, Y. B. Spin-triplet pairing instability of the spinon fermi surface in
 495 a U(1) spin liquid. *Phys. Rev. Lett.* **99**, 266403 (2007).
 496 42 Grover, T., Trivedi, N., Senthil, T. & Lee, P. A. Weak Mott insulators on the
 497 triangular lattice: Possibility of a gapless nematic quantum spin liquid. *Phys. Rev. B*
 498 **81**, 245121 (2010).
 499 43 Xu, X. Y., Law, K. T. & Lee, P. A. Pair Density Wave in the Doped t - J Model with
 500 Ring Exchange on a Triangular Lattice. *Phys. Rev. Lett.* **122**, 167001 (2019).
 501 44 Agterberg, D. F. & Tsunetsugu, H. Dislocations and vortices in pair-density-wave
 502 superconductors. *Nature Phys.* **4**, 639-642 (2008).
 503 45 Fradkin, E., Kivelson, S. A. & Tranquada, J. M. Colloquium: Theory of intertwined
 504 orders in high temperature superconductors. *Rev. Mod. Phys.* **87**, 457-482 (2015).
 505 46 Tang, E., Fisher, M. P. A. & Lee, P. A. Low-energy behavior of spin-liquid electron
 506 spectral functions. *Phys. Rev. B* **87**, 045119 (2013).
 507 47 Edkins, S. D. *et al.* Magnetic field-induced pair density wave state in the cuprate
 508 vortex halo. *Science* **364**, 976 (2019).
 509 48 Huse, D. A. & Elser, V. V. Simple variational wave functions for two-dimensional
 510 Heisenberg spin-1/2 antiferromagnets. *Phys. Rev. Lett.* **60**, 2531-2534 (1988).
 511 49 Ribeiro, P. & Lee, P. A. Magnetic impurity in a U(1) spin liquid with a spinon Fermi
 512 surface. *Phys. Rev. B* **83**, 235119 (2011).
 513 50 Norman, M. R. & Micklitz, T. How to measure a spinon fermi surface. *Phys. Rev. Lett.*
 514 **102**, 067204 (2009).
 515
 516
 517

518 **Fig. 1. Structure of single-layer TaSe₂ and 1T/1H vertical heterostructures.**

519 **a**, Side-view of the crystal structures of single-layer 1T- and 1H-TaSe₂ as well as a 1T/1H
520 vertical heterostructure on BLG-terminated SiC(0001). **b**, STM topographic image shows
521 single-layer 1T-TaSe₂, single-layer 1H-TaSe₂, and a 1T/1H vertical heterostructure on
522 BLG/SiC(0001) ($V_b = -1$ V, $I_t = 5$ pA). The insets are close-up images of the single-layer 1T
523 and 1H islands (scanned at $V_b = -0.5$ V, $I_t = 30$ pA, and $V_b = 50$ mV, $I_t = 1.3$ nA, respectively)
524 ($T = 5$ K). **c**, Schematic of the triangular spin lattice and star-of-David charge density wave
525 pattern in 1T-TaSe₂. Each star consists of 13 Ta atoms and has a localized spin represented
526 by a blue arrow at the star center. The wavefunction of the localized electrons is represented
527 by gray shading.

528 **Fig. 2. Kondo resonance observed in a 1T/1H TaSe₂ vertical heterostructure.**

529 **a**, Local electronic structure measured at $T = 5$ K via dI/dV spectroscopy for single-layer 1H-
530 TaSe₂ (green), single-layer 1T-TaSe₂ (red), and a 1T/1H TaSe₂ vertical heterostructure (blue)
531 (1H: $V_b = -1.5$ V, $I_t = 30$ pA, $V_{\text{mod}} = 50$ mV; 1T: $V_b = 1.5$ V, $I_t = 40$ pA, $V_{\text{mod}} = 20$ mV; 1T/1H:
532 $V_b = -1.5$ V, $I_t = 30$ pA, $V_{\text{mod}} = 20$ mV). The insets show higher resolution dI/dV spectra (1H:
533 $V_b = 0.1$ V, $I_t = 30$ pA, $V_{\text{mod}} = 5$ mV; 1T: $V_b = -0.25$ V, $I_t = 30$ pA, $V_{\text{mod}} = 2$ mV; 1T/1H: $V_b =$
534 -0.1 V, $I_t = 30$ pA, $V_{\text{mod}} = 1$ mV) (the Kondo peak in the inset is sharper and taller compared
535 to the lower resolution measurement due to the use of a smaller wiggle voltage). **b**,
536 Temperature dependence of the Kondo resonance peak observed in 1T/1H TaSe₂ vertical
537 heterostructures for $5 \text{ K} \leq T \leq 70 \text{ K}$. The spectra are vertically offset for clarity ($V_b = -0.1$ V,
538 $I_t = 30$ pA, $V_{\text{mod}} = 1$ mV). **c**, Temperature dependence of the intrinsic Kondo resonance width
539 Γ (black with error bar). The error is estimated by the Γ threshold beyond which the fit
540 significantly worsens³⁷. The fit of Eq. (1) to the data (red dashed line) yields a Kondo
541 temperature of $T_K = 57$ K.

542 **Fig. 3. Super-modulations in single-layer 1T-TaSe₂ visualized by spectroscopic imaging.**

543 **a**, Large-scale topographic image of a single-layer 1T-TaSe₂ island ($V_b = -1$ V, $I_t = 2$ pA). **b**,

544 The dI/dV spectrum of single-layer 1T-TaSe₂ ($V_b = 1.5$ V, $I_t = 40$ pA, $V_{\text{mod}} = 20$ mV). **c-g**,

545 Constant-height dI/dV maps at different energies acquired in the area indicated by yellow

546 dashed square in **a** ($I_t = 30$ pA, $V_{\text{mod}} = 20$ mV). **h-i**, Corresponding Fourier transforms (FTs)

547 of the dI/dV maps in **c-g**. FT peaks circled in red reflect the primary reciprocal lattice vectors

548 of the star-of-David CDW and the red hexagon represents the CDW Brillouin zone. FT peaks

549 circled in blue (**i-k**) reflect the incommensurate super-modulation (ICS) at 0.62 V, 0.2 V, and

550 -0.18 V. FT peaks circled in green (**k**) reflect the commensurate super-modulation (CS) ($T =$

551 5 K).

552 **Fig. 4. Energy dependence of super-modulations in single-layer 1T-TaSe₂.**

553 **a**, Plot of Fourier transform (FT) amplitude as a function of both the wavevector $\mathbf{q} =$

554 $q(\mathbf{b}_1 + \mathbf{b}_2)$ (q measured in units of $|\mathbf{b}_1 + \mathbf{b}_2| = 4\pi/a$) along the Γ -K direction (y -axis, indicated

555 by black dashed line in the inset) and the sample bias voltage (x -axis). High FT amplitude

556 (dark color) appears at $\mathbf{b}_1 + \mathbf{b}_2$ (black dashed ovals), the ICS wavevector (blue dashed ovals),

557 and the CS wavevector (green dashed oval) ($T = 5$ K). **b**, Energy dependence of the ICS

558 strength (blue dots) shows enhanced amplitude at Hubbard band energies. The ICS strength is

559 defined as the FT amplitude at the ICS wavevector ($\rho(E, \mathbf{q}_{\text{ICS}})$) divided by the FT amplitude

560 at $\mathbf{q} = \mathbf{0}$ ($\rho(E, \mathbf{q} = \mathbf{0})$). The reference dI/dV spectrum is plotted in black ($T = 5$ K). **c**,

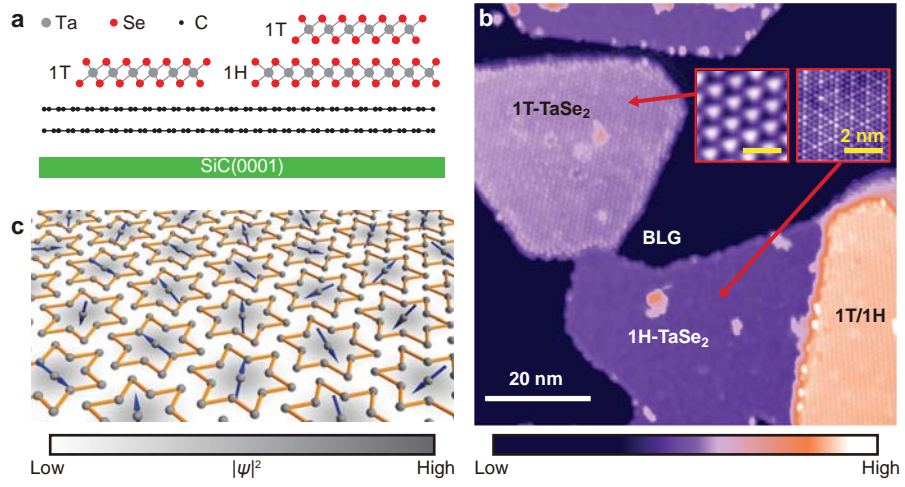
561 Schematic density of states of a Mott insulator. **d**, Cartoon of a tip-QSL tunnel junction. An

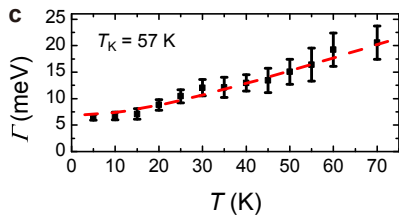
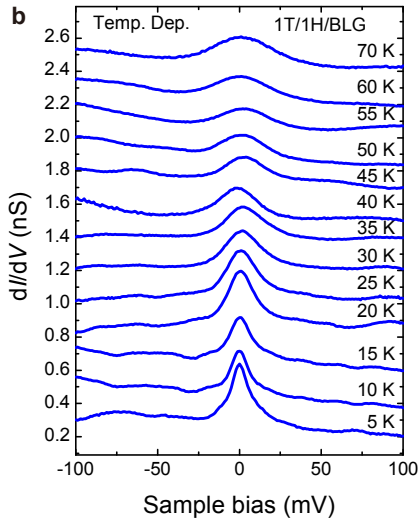
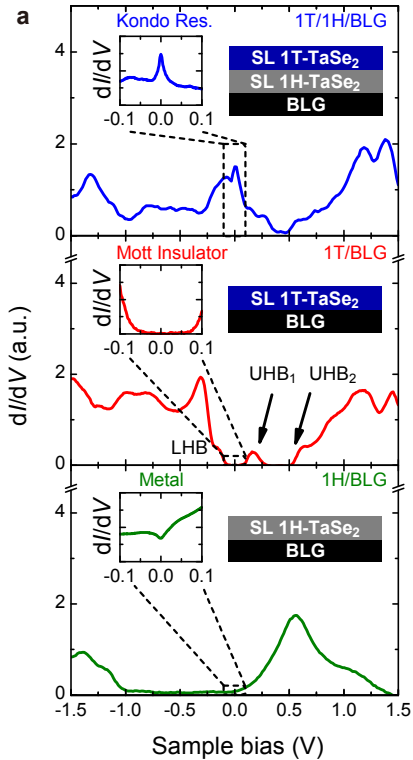
562 electron injected into the strongly-correlated UHB of the QSL decays into a spinon and a

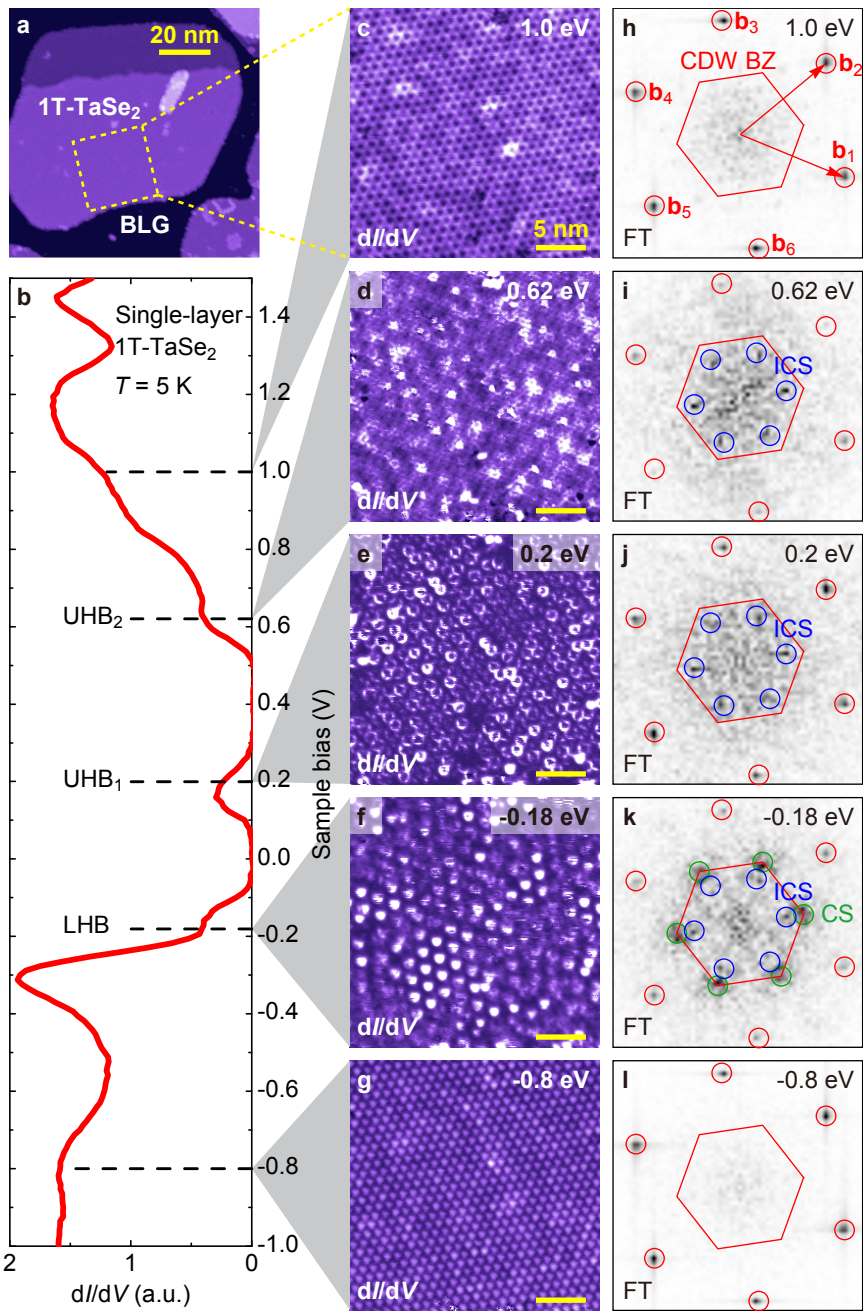
563 chargon.

564 **Fig. 5. Super-modulation periodicities predicted from spinon Fermi surface compared**
565 **with experiment.**

566 **a**, Schematic of spinon Fermi surface at half-filling (red) with partial gaps opening along the
567 Γ -M directions. The black hexagon is the star-of-David CDW Brillouin zone and the black
568 arrows (\mathbf{b}_i) are the primary reciprocal lattice vectors of the CDW Brillouin zone ($1 \leq i \leq 6$,
569 only \mathbf{b}_1 and \mathbf{b}_2 are labeled). The spinon Fermi surface instability wavevectors \mathbf{P}_i (red arrow)
570 connect the partial gaps on different spinon Fermi surfaces in an extended zone scheme. **b**,
571 Spinon Fermi surface instability wavevectors \mathbf{P}_i (red dots) and harmonics \mathbf{Q}_i (blue dots) and
572 \mathbf{Q}'_i (purple dots) in the CDW Brillouin zone. **c**, Fourier transform (FT) of the STM image of
573 1T-TaSe₂/BLG at $V_b = 0.5$ V (STM image shown in Supplementary Fig. 7a inset).
574 Experimental ICS wavevectors \mathbf{q}_{ICS} are circled in blue ($T = 5$ K). **d**, FT of the STM image of
575 1T-TaSe₂/HOPG at $V_b = -0.15$ V (STM image shown in Supplementary Fig. 12j).
576 Experimental super-modulation wavevectors \mathbf{q}_M close to the M points are circled in purple (T
577 $= 5$ K).







Sample bias (V)

